Effective indirect exchange interaction in *p*-doped MoS_2 nanoribbons in the presence of intrinsic spin-orbit interaction

Akram Mirehi and Ebrahim Heidari-Semiromi*
Department of Physics, University of Kashan, Kashan 87317-53153, Iran

(Received 4 March 2019; revised manuscript received 3 May 2019; published 22 July 2019)

We study the Ruderman-Kittel-Kasuya-Yosida (RKKY) coupling between localized magnetic impurities in the MoS_2 nanoribbons. Our calculations are based on a three-orbital tight-binding model for a MoS_2 finite nanoribbon system with periodic boundary conditions. We consider impurities hybridized to different d orbitals of the host transition metal. The large intrinsic spin-orbit coupling leads to the spatial anisotropy in the RKKY interaction amplitude and appearance of collinear and noncollinear terms. We find that the RKKY interaction is sensitive to the Fermi energy values and changes dramatically in doped systems. We analyze the exponent decay behavior of the RKKY interaction envelope for doping levels inside the band gap of the infinite layer.

DOI: 10.1103/PhysRevB.100.035425

I. INTRODUCTION

Two-dimensional (2D) layered materials in particular transition-metal dichalcogenides (TMDs) such as MoS_2 and WSe_2 have gotten attention recently [1]. TMDs have the chemical composition of type MX_2 which consists of three atomic layers. M is one layer of the transition metal of groups 4–10, which is sandwiched between two chalcogen X layers. Among the various TMDs, the group-VIB ones (WSe_2, MoS_2) as a new class of semiconductors have direct band gap in the visible frequency range [2] and also have different electronic structure such as strong photoluminescence, large spin-orbit coupling (SOC) [3,4]. A variety of methods have been prepared samples of thin group-VIB TMDs (monolayers, bilayers, etc.) including mechanical exfoliation [5], chemical exfoliation [6], physical vapor deposition (PVD) [7], and chemical vapor deposition (CVD) [8–10].

MoS_2, a semiconductor of the TMD family, with its remarkable thermal and chemical stability and high mobility is one of the most studied 2D materials [11–14]. Recent theoretical and experimental studies have been focused on the electrical, mechanical, and optical properties of the MoS_2 monolayer [6,15–19]. The MoS_2 monolayer exhibits other unique properties than its bulk configuration. For instance, bulk MoS_2 is an indirect-gap semiconductor with a band gap of 1.29 eV, while the MoS_2 monolayer is found to be semiconducting with a band gap of 1.8 eV [20]. Due to the relevant admixture of Mo d orbitals, MoS_2 has a relative strong spin-orbital coupling and is a good candidate for the applications of spintronic devices [14]. The pristine bulk MoS_2 is nonmagnetic, while recent studies have been found that MoS_2 nanostructures are magnetic due to zigzag edges or vacancies [21,22]. Considerable efforts have been focused on low-dimensional MoS_2 nanostructures which are suitable candidates for spintronics [23], catalysts [24,25], solar cells [26], and Li-ion batteries applications [27]. MoS_2 zigzag nanoribbons have been investigated by using the density functional theory approach. These nanostructures could be metallic and could exhibit a surprising ferromagnetic behavior due to edge states [28,29].

Ruderman-Kittle-Kasuya-Yosida (RKKY) interaction is an indirect interaction between localized magnetic impurities in the host material via the conduction electrons. The RKKY interaction has been studied in infinite graphene [30], graphene nanoribbons [31–33], graphene nanoflakes [34,35], TMDs monolayers [36–38], and TMDs nanoflakes [39,40]. Interaction (RKKY) in TMDs which have a complex band structure and also have orbital degrees of freedom and strong intrinsic spin-orbit interactions is more complex than conventional metals. In TMDs, the effect of the SOC on the anisotropic magnetic exchange interaction is particularly important because the spin-orbit coupling (SOC) produces a large spin splitting near the valence band maximum [40]. The study of RKKY interaction between impurities in the presence of SOC in this energy region is more noticeable and controllable. The electronic properties of TMDs infinite monolayers in the presence of a large variety of impurities such as Mn [41–44], Fe [41–45], Co [14,41–43], V [43,46], Nb [43,46], and Ta [43] have been investigated by using first-principles density functional theory (DFT). The RKKY interaction on *p*-doped triangular zigzag-terminated MoS_2 nanoflakes with the impurities localized on the edges of the flake has been studied and also the dependence of the interaction of hole doping is investigated by using an effective three-orbital tight-binding model [39,40].

The substitutional impurities such as Nb and Mn with Mo for *p*-doped MoS2 have been investigated [41,47]. We analyze the RKKY interaction for *p*-doped MoS_2 nanoribbons in the presence of the SOC with different Fermi levels at midgap energies. Two magnetic impurities are localized at onsite or plaquette positions. The onsite impurities are hybridized on top of single transition-metal atoms, while the plaquette impurities are localized in hollow sites of transition-metal triangles. By switching on the SOC, the symmetry breaking occurs and RKKY interaction between localized spins

*eb.heidari@gmail.com

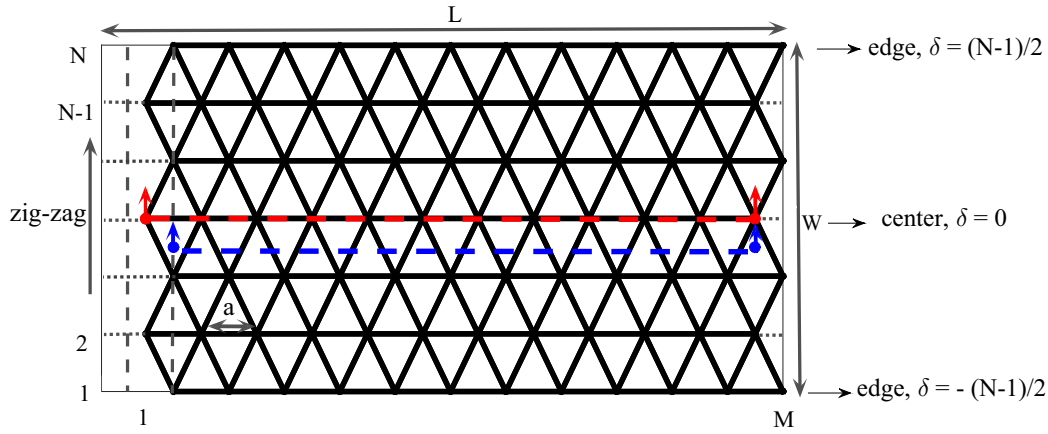

FIG. 1. Schematic view of a MoS_2 nanoribbon system used with width W and length L. This system includes N atoms of Mo at the vertical edge and M atoms at the horizontal edge. The gray dashed lines surround a single row of atoms in the zigzag direction of the nanoribbon, so that periodic boundary conditions contain zigzag atomic rows as $M + 1 = M$. The symmetry axis of the nanoribbon which is shown by a red dashed line corresponds to $\delta = 0$. The edges of the nanoribbon are shifted by $\delta = \pm(N-1)/2$ direct lines from the center. The first impurity is held fixed while the second impurity moves along the symmetry axis, as shown by the dashed red in the onsite case and the dashed blue in the plaquette case.

consists of three different terms: Heisenberg, Dzyaloshinsky-Moriya, and Ising interactions. Using an effective three-orbital tight-binding model, we perform the exact diagonalization of the single-particle Hamiltonian. We investigate the role of separation between impurities on the intensity of the coupling, comparing the behavior of impurities along the symmetry axis of the nanoribbon and on edges. The Ising interaction shows the larger period of oscillation compared to the other terms at the deeper Fermi level in the gap, which is explained by intervalley scattering processes. We also analyze the nanoribbon width dependence on the coupling for the fixed distance between the impurities. We explore a beating pattern of oscillations of the RKKY interaction which depends strongly on the direction of impurity separation and decays exponentially by increasing distance.

II. MODEL AND HAMILTONIAN

We study a finite system of the MoS_2 nanoribbon with periodic boundary conditions as shown in Fig. 1, schematically. We consider the sample with N row and M column of metal atoms, so the total number of sites contains $M.N$. The width of the MoS_2 nanoribbon is defined as the number of direct lines across the nanoribbon width, while the length of the MoS_2 nanoribbon is defined as the number of zigzag lines along the direction parallel to the nanoribbon zigzag edges. The nearest-neighbor distance equals to $a = 3.19$ Å. The corresponding length of the nanostructure is $L = Ma$, while its width is $W = \sqrt{3/2}(N-1)a$. The nanoribbon has the symmetry axis which is described by $\delta = 0$ and the nanoribbon edges are shifted by $\delta = \pm(N-1)/2$ direct lines from the center. Three Mo d orbitals containing d_{z^2}, d_{xy}, and $d_{x^2-y^2}$ contribute significantly. The full Hamiltonian of the system including two magnetic impurities can be written as:

$$H = H_0 + H_{\rm imp}, \tag{1}$$

where $H_0 = H_{\rm on} + H_{\rm SOC} + H_t$ describes TMD without impurities, and $H_{\rm imp}$ is the interaction term between impurities and spin of conduction electrons. The onsite Hamiltonian is given by:

$$H_{\rm on} = \sum_{j=1}^{N_t} \sum_{\sigma=\uparrow,\downarrow} \sum_{\alpha,\alpha'} \varepsilon_{\alpha,\alpha',\sigma} c^{\dagger}_{\alpha,\sigma}(r_j) c_{\alpha',\sigma}(r_j), \tag{2}$$

where, $c^{\dagger}_{\alpha,\sigma}(r_j)$ $[c_{\alpha',\sigma}(r_j)]$ is the creation (annihilation) operator of the conduction electrons at lattice site $r_j = j_1 a_1 + j_2 a_2$ of the nanoribbon with orbital d_α and spin $\sigma = \uparrow, \downarrow$. The a_l are lattice vectors, $a_1 = a(1, 0)$, $a_2 = a(1/2, \sqrt{3}/2)$, with lattice constant a. $\alpha \in \{z^2, xy, x^2 - y^2\}$ and $\varepsilon_{\alpha,\alpha',\sigma}$ are the onsite energies [48]. The nearest-neighbors hopping Hamiltonian is given by:

$$H_t = \sum_{j,\sigma,\alpha,\alpha'} \sum_{l=1}^{3} t^{(a_l)}_{\alpha,\alpha'} c^{\dagger}_{\alpha,\sigma}(r_j) c_{\alpha',\sigma}(r_j + a_l) + \text{H.c.}, \tag{3}$$

where $t^{(a_l)}_{\alpha,\alpha'}$ are hopping parameters in the three nearest-neighbor directions, $j = 1, 2, 3$. The different onsite energies and hopping parameters are taken from [48–50].

Using the theoretical studies [51,52] and first-principle calculations [53–56], it is known that the valence and the conduction bands are made mostly from d_{z^2}, d_{xy}, and $d_{x^2-y^2}$ orbitals, while the contributions from s and p orbitals are small in these bands. Thus in the tight-binding method, a suitable approximation is to consider only the onsite contribution of Mo atoms with three d orbitals. We consider SOC interaction through the approximation of onsite MO contributions as $H_{\rm SOC} = \lambda L_z S_z$ which can be written as in terms of creation and annihilation operators of the electrons as:

$$H_{\rm soc} = \lambda/2 \sum_{j=1}^{N_t} \sum_{\sigma=\uparrow,\downarrow} \sum_{\alpha,\alpha'} (L_z)_{\alpha,\alpha'} (\sigma_z)_{\alpha,\alpha'} c^{\dagger}_{\alpha,\sigma}(r_j) c_{\alpha',\sigma}(r_j), \tag{4}$$

in which:

$$L_z = \begin{bmatrix} 0 & 0 & 0 \\ 0 & 0 & 2i \\ 0 & -2i & 0 \end{bmatrix}.$$

L_z is the z component matrix of the orbital angular momentum, S_z is the spin Pauli matrix, and λ is the SOC strength. By considering the bases $\{|d_{z^2},\uparrow\rangle, |d_{xy},\uparrow\rangle\}, |d_{x^2-y^2},\uparrow\rangle, |d_{z^2},\downarrow\rangle, |d_{xy},\downarrow\rangle\}, |d_{x^2-y^2},\downarrow\rangle$, we get components of the SOC contribution, including $\varepsilon_{d_{xy}d_{x^2-y^2},\uparrow} = \varepsilon_{d_{x^2-y^2}d_{xy},\downarrow} = i\lambda$, $\varepsilon_{d_{xy}d_{x^2-y^2},\downarrow} = \varepsilon_{d_{x^2-y^2}d_{xy},\uparrow} = -i\lambda$. We consider $2\lambda = 150$ meV reported in previous works of density functional theory (DFT) calculations and the experimental values [57–60].

We consider two magnetic impurities hybridized to Mo atoms, since at low energies (near the optical gap) admixtures of d orbitals from these atoms mainly contribute the most to the states. $H_{\rm imp}$ is the Anderson-Kondo term between the magnetic impurities and spins of the conduction electrons:

$$H_{\rm imp} = \sum_{i=1,2} \frac{J_{\alpha_i}}{2} S_i^{\rm imp}.s_{\alpha_i}(r_i), \tag{5}$$

where J_{α_i} shows the coupling between the magnetic impurity spins i and the conduction electrons at the specific sites of the TMD lattice and orbital α (d_{z^2}, d_{xy} or $d_{x^2-y^2}$). We set $J_\alpha = 0.3$ meV [39] and consider that the exchange coupling J is the same for both impurities, irrespective of the orbital to which they hybridize. The value of J_α is a choice in accordance with predictions that range from a few meV to a couple hundred meV [44–46,61], even at the edges [62]. $S_i^{\rm imp}$ is the spin operator of the localized magnetic impurity i, and $s_{\alpha_i}(r_i)$ is the electron spin operator at site (r_i) for orbital α_i.

$$s_\alpha(r) = \sum_{\sigma,\sigma'=\uparrow,\downarrow} \langle\sigma|s_\alpha|\sigma'\rangle c^\dagger_{\alpha,\sigma}(r) c_{\alpha,\sigma'}(r), \tag{6}$$

where σ is the vector of spin-1/2 Pauli matrices. Substituting equation (6) in equation (5), the RKKY interaction by using a second-order perturbation [63–66] can be read as:

$$H_{\rm imp} = \frac{J_{\alpha_1}}{2} \sum_{\beta=x,y,z} S_1^{(\beta)} \sum_{\sigma,\sigma'=\uparrow,\downarrow} \langle\sigma|s_{\alpha 1}^{(\beta)}|\sigma'\rangle c^\dagger_{\alpha_1,\sigma} c_{\alpha_1,\sigma'} + \frac{J_{\alpha_2}}{2} \sum_{\beta=x,y,z} S_2^{(\beta)} \sum_{\sigma,\sigma'=\uparrow,\downarrow} \langle\sigma|s_{\alpha 2}^{(\beta)}|\sigma'\rangle c^\dagger_{\alpha_2,\sigma} c_{\alpha_2,\sigma'}, \tag{7}$$

where β and β' represent the spin projection $(x;y;z)$ for first and second magnetic impurities, respectively. The effective anisotropic spin interaction between localized magnetic moments includes Ising J_{ZZ}, $J_{XX}(=J_{YY})$ and J_{DM} Dzyaloshinskii-Moriya (DM) interactions. The RKKY Hamiltonian can be expressed as:

$$H^{\rm RKKY} = J_{XX}\left(S_1^x S_2^x + S_1^y S_2^y\right) + J_{ZZ}\left(S_1^z S_2^z\right) + J_{DM}(S_1 \times S_2)_z. \tag{8}$$

The ground state energy in a nanostructure for both parallel and antiparallel orientation of the impurity spins is defined as the sum of the sorted energy states of the full Hamiltonian up to the Fermi energy ε_F, $E(S^1_{\rm imp}, S^2_{\rm imp}) = \sum_{\uparrow,\downarrow} \sum_{i=1}^{\varepsilon_F} \varepsilon_{i,\sigma}$, where the electronic eigenstates $\varepsilon_{i,\sigma}$ of the system are found by diagonalization of the full Hamiltonian H, described by a

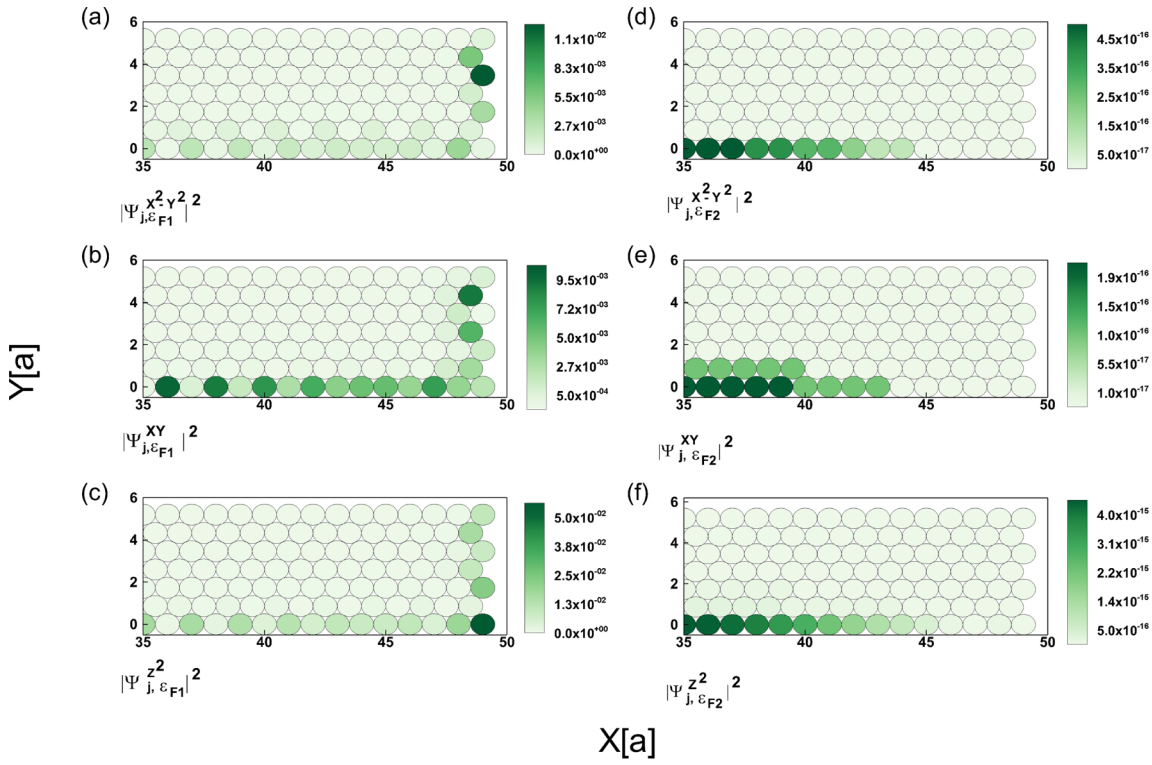

FIG. 2. The magnitude squared of the wave function, $|\psi_{j,\varepsilon_{F_i}}|^2$ $(i = 1, 2)$, for the three different orbitals for the right-hand side of nanoribbon. The results correspond to two doping levels (a)–(c) ε_{F_1} and (d)–(f) ε_{F_2}, as indicated in each panel.

matrix of size $6N_t \times 6N_t$.

$$E\left(S^{(\beta)}_{(\alpha)} = \uparrow, S^{(\beta')}_{(\alpha')} = \downarrow\right) - E\left(S^{(\beta)}_{(\alpha)} = \uparrow, S^{(\beta')}_{(\alpha')} = \uparrow\right) = 2S^2 J^{(\beta,\beta')}_{(\alpha,\alpha')}. \tag{9}$$

The negative (positive) values of J correspond to ferromagnetic [antiferromagnetic (AFM)] coupling between the magnetic moments.

III. RESULTS AND DISCUSSION

We consider p-doped MoS_2 nanoribbon system of 50 rows (approximately 160 Å). The values of width N used in the calculations of distance dependence of the coupling are odd. We use $\varepsilon_{F_1} = 0.4793\,\text{eV}$ and $\varepsilon_{F_2} = 0.2180\,\text{eV}$, corresponding to 52 and 106 holes in the nanoribbon. Two magnetic impurities are hybridized to d orbitals of the Mo atoms in the nanocrystal. For instance, $J_{x^2-y^2,x^2-y^2}$ is the interaction strength between impurities when the first and second impurities are hybridized both to $d_{x^2-y^2}$ orbitals. The RKKY interaction has the different oscillatory pattern, depending on different doping levels and also the orbital to which impurities hybridize. Figure 2 represents the normalized wave functions in real space, $|\psi_{j,\varepsilon_{F_i}}|^2$ $(i = 1, 2)$, for the corresponding unperturbed MoS_2 nanoribbon for Fermi levels fixed at two different p-doped levels, corresponding to 52 and 106 holes. Two Fermi levels are shown in the insets of Fig. 2. We consider the right-hand side of MoS_2 nanoribbon. We can see that for ε_{F_1} the wave functions are mostly localized at the Lower edge and zigzag edge of the nanoribbon, while for ε_{F_2} the wave functions are localized at the lower edge with much smaller amplitudes. As the Fermi energy gets deeper into the valence band, such as ε_{F_2}, the square magnitude of wave function becomes smaller. Thus, we can control the strength of the indirect interaction by localizing the impurities at points where the modulus squared of the wave function has large amplitudes.

As a general rule, the exchange interaction decays as $(2k_F r)^2\cos(2k_F r)$ in conventional metals [67,68]. This spatial pattern is a combination of an oscillatory function $\cos(2k_F r)$ and a decaying envelope $[(2k_F r)^2, d < 0]$, where r is the distance between two impurities, k_F is the Fermi wave vector, and $|d|$ is the dimensionality of the host material. The oscillatory term $\cos(2k_F r)$ changes the behavior of the interaction between FM and AFM alignment. The intriguing manner of the RKKY interaction in doped MoS_2 finite-length nanoribbon is its dependence on the Fermi energy values which in turn changes by the level of doping. The RKKY interaction by definition is due to the conduction electrons the density of which is determined by the density of states (DOS) at the Fermi energy. The long-range (exponential decay) RKKY coupling in MoS_2 nanoribbon is in contrast to the short-range (r^{-3} decay) in the bulk because of the extreme easiness of polarizing and unpolarizing the localized edge states of the MoS_2 nanoribbon. On the other hand, the spin and orbital content of the conduction states and symmetry of the host state electrons influence the resulting value of indirect interaction features. For instance, in graphene, the interaction decays as r^{-3} at the Dirac point, while in doped or spin-polarized graphene it decays with the distance according to r^{-2} [36], as in conventional 2D materials. In MoS_2 nanoflakes, the exchange interaction decays with $|d| < 2$ for doping levels inside the band gap of the infinite layer, corresponding to edge states of the flake at the Fermi level and exhibit sub-2D

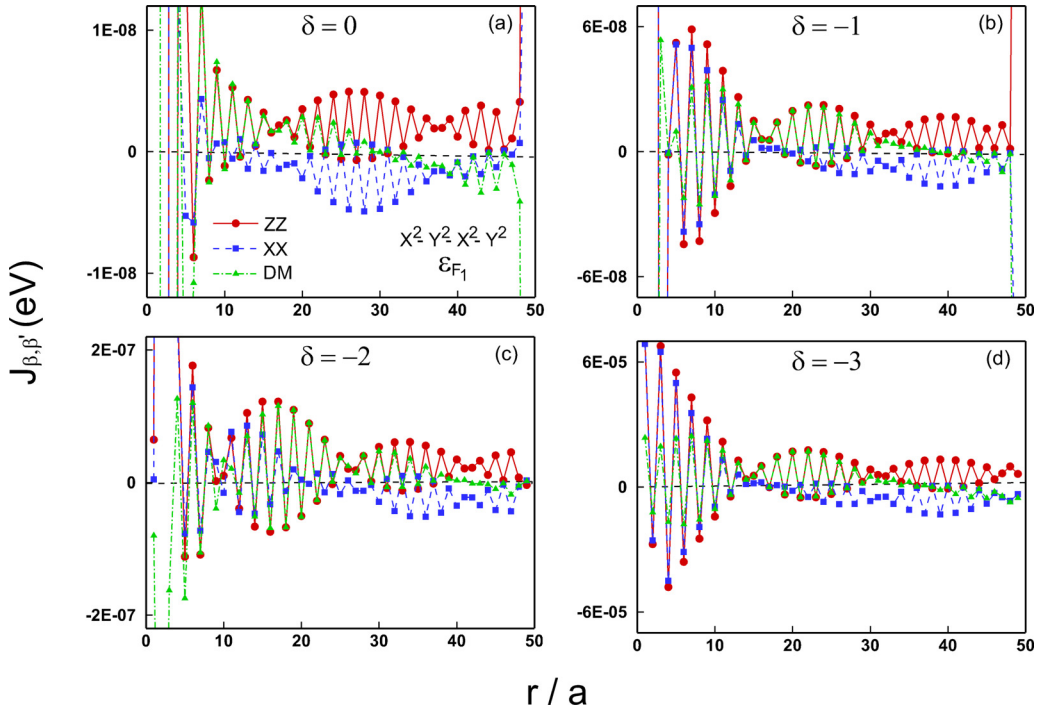

FIG. 3. The three components of the effective impurity interaction vs relative distance along the horizontal directions of the nanoribbon. All curves correspond to ε_{F1}. The plots are presented for various distances of the impurities from the nanoribbon center ($\delta = 0, -1, -2, -3$). The first impurity is fixed at the begin of the selected row, while the second one moves at all onsites along the corresponding direction. First and second impurities are assumed hybridized both to $d_{x^2-y^2}$ orbitals which are indicated in panel (a).

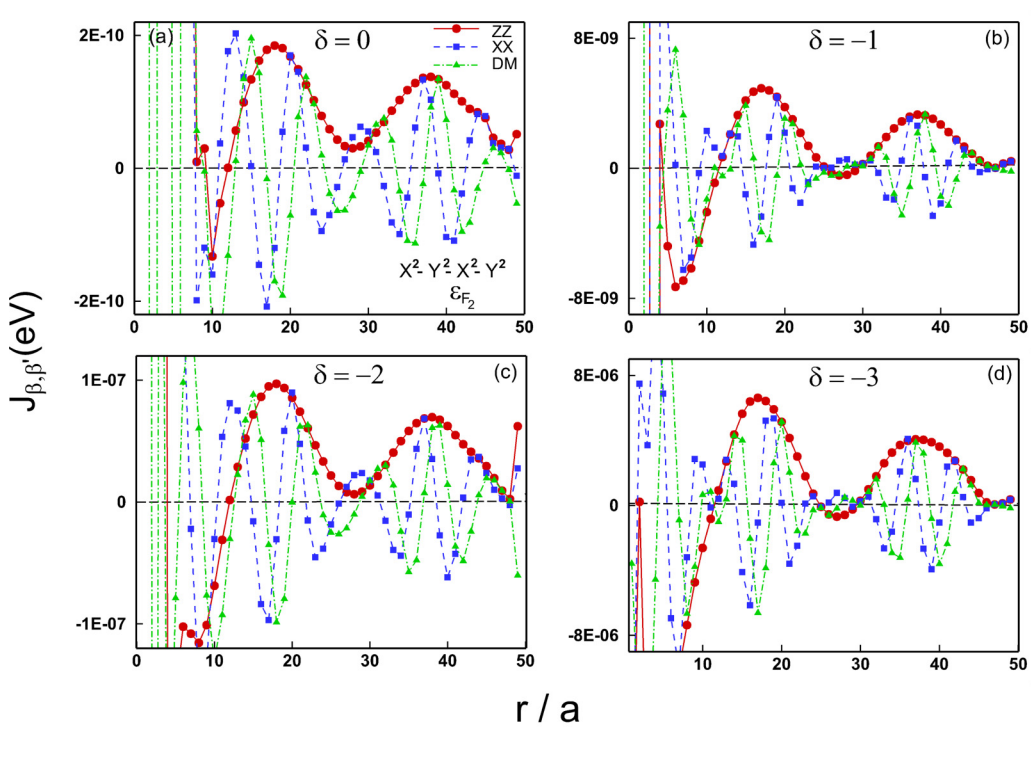

FIG. 4. The three components of the effective impurity interaction vs relative distance along the horizontal directions of the nanoribbon. All curves correspond to ε_{F2}. The plots are presented for various distances of the impurities from the nanoribbon center ($\delta = 0, -1, -2, -3$). The first impurity is fixed at the beginning of the selected row, while the second one moves at all onsites along the corresponding direction. First and second impurities are assumed hybridized both to $d_{x^2-y^2}$ orbitals which are indicated in panel (a).

decay behavior [40]. We analyze the distance dependence for the indirect coupling between magnetic impurities in MoS_2 nanoribbons for doping levels lying inside the band gap, comparing the behavior of impurities along the symmetry axis and on edges.

In Fig. 3, the distance dependence of the RKKY coupling between magnetic impurities for MoS_2 nanoribbon with the width of $N = 7$ for different distances of the impurity pair from the nanoribbon center is presented. The first impurity is fixed at an initial position on the zigzag edge in the nanoribbon center or with distance ($\delta = -1, -2, -3$) from the nanoribbon center. The second impurity is moved along the symmetry axis. Two impurities, as indicated in the inset (a), are hybridized to $d_{x^2-y^2}$ orbitals for doping level ε_{F_1}, corresponding to 52 holes. The largest distance between the magnetic impurities considered in this paper is $r/a = 49$. The three components (Ising, XX, and DM) oscillate between antiferromagnetic (AFM) ($J > 0$) and ferromagnetic (FM) ($J < 0$) as the impurities separate. The different terms exhibit similar behavior of oscillation. In panels (a) and (b), $J_{ZZ} > 0$ for $r/a > 30$, so that for large distances between the impurities the behavior of the Ising interaction does not change from F to AF magnetic order or vice versa and thus polarization of impurity spins is AFM with respect to the interactions J_{XX} and J_{DM} which are almost FM as the impurities separate. In general, interaction J_{ZZ} is out of phase with J_{XX} and J_{DM}, however, J_{ZZ} and J_{DM} are in phase with each other for some separation, for instance for $15 < r/a < 30$ in the panels (b), (c), and (d). We can see that for impurities located in the center of the nanoribbon, in panel (a), Ising J_{ZZ} has a larger period of oscillation than other panels. The strength of the RKKY coupling between the edge impurities, panel (d), is stronger than center impurities, panel (a).

In Fig. 4, we have plotted results corresponding to Fig. 3, but for doping level ε_{F_2}, corresponding to 106 holes. Two magnetic impurities are hybridized to $Mo\ d_{x^2-y^2}$ orbitals and the various distances of the impurities from the nanoribbon center are considered, $\delta = 0, -1, -2, -3$, like Fig. 3. We find the different oscillatory pattern for exchange interactions in comparison to the one described for ε_{F_1}. In contrast to the J_{XX} and J_{DM} terms, with a period of $\simeq$7 sites, Ising J_{ZZ} has a long-period oscillation with a period of $\simeq$20 sites.

This behavior can be attributed to the fact that for J_{ZZ} intervalley scattering differs from J_{XX} and J_{DM} according to the achievements of Ref. [48]. As one can observe, J_{ZZ} is dominated due to scattering processes that happens within the same K or K' valley, without spin flip introduced. J_{XX} and J_{DM} terms show a shorter oscillation period than J_{ZZ} because intervalley scattering processes occur from K valley to K' or Γ (and vice versa), which flip the spin. Although J_{XX} and J_{YY} change sign every 3–5 sites, J_{ZZ} is mostly AFM (positive) in nature, with a small FM in the interval $r/a \in [25, 30]$ in panels (b) and (d) and $r/a < 12$ in each panel. In general, the constant amplitude of the oscillations of the RKKY coupling between magnetic impurities shows an envelope exponent. The three components of interactions

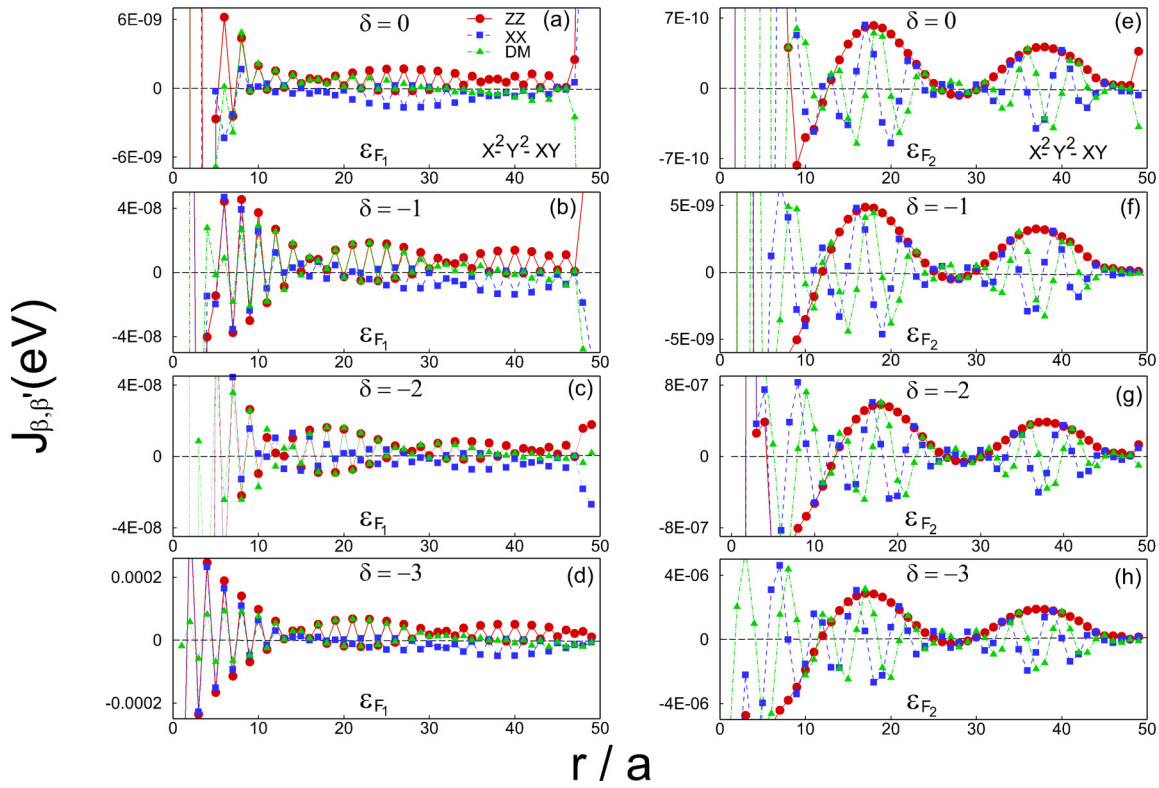

FIG. 5. The three components of the effective impurity interaction vs relative distance along the horizontal directions of the nanoribbon. The curves correspond to ε_{F1}, panels (a)–(d), and ε_{F2}, panels (e)–(h). The plots are presented for various distances of the impurities from the nanoribbon center ($\delta = 0, -1, -2, -3$). The first impurity is connected to $d_{x^2-y^2}$ and the second to d_{xy} orbitals. The first impurity is fixed at the beginning of the selected row, while the second one moves at all onsites along the corresponding direction.

are out of phase with each other, although J_{XX} and J_{DM} terms have a relative phase difference of nearly one site between themselves. However, Ising component has the same phase with J_{XX} or J_{YY} terms for some impurity separations, for instance with J_{XX} for $r/a = 19$ and with J_{DM} for $r/a = 44$ in panel (b). By increasing the distance between the magnetic impurities, the RKKY coupling decays slower with respect to Fig. 3, for ε_{F_1}. The coupling for edge impurities increases approximately four orders of magnitude with respect to the impurities of the nanoribbon center. By comparison of Figs. 3 and 4, it is observed that the coupling terms for ε_{F_1}, lower doping level, have greater values than ε_{F_2}.

In Fig. 5, we have plotted the indirect exchange versus the distance between impurities when the first impurity is connected to the $d_{x^2-y^2}$ orbital and the second one to the d_{xy} orbital. The interactions which are shown for ε_{F_1} in panels (a)–(d) and for ε_{F_2} in panels (e)–(h) have similar oscillation behavior to the one described for $J^{x^2-y^2,x^2-y^2}$ with natural quantitative differences on the overall amplitude, that depend on the orbital to which impurities hybridize. The interaction $J^{x^2-y^2,xy}$ for ε_{F_2} has the same order of magnitude as $J^{x^2-y^2,x^2-y^2}$, while for ε_{F_1} is typically 10 times smaller in magnitude due to the second impurity hybridized to a d_{xy} orbital. We can see that $J^{x^2-y^2,xy}$ for ε_{F_1} has a shorter period of oscillation, about 15 sites, than $J^{x^2-y^2,x^2-y^2}$ in Fig. 3, while for ε_{F_2} exhibits the similar oscillatory pattern in comparison to $J^{x^2-y^2,x^2-y^2}$ in Fig. 4. If we compare the $J^{x^2-y^2,xy}$ behavior for two different levels of hole doping in panels (a)–(h), we observe that the Ising interaction for ε_{F_1} has a shorter oscillation period than ε_{F_2}, by a typical factor of 1 or 2 times larger in magnitude. Also, we can see that the decay behavior of the RKKY interaction envelope with distance for ε_{F_1} is faster than ε_{F_2}. Thus the interaction decays slower for deeper Fermi levels in the gap (higher doping). This result also is achieved for MoS_2 nanoflakes, recently [39]. The coupling for edge impurities is larger than for center impurities by approximately 5 and 4 orders of magnitude for ε_{F_1} and ε_{F_2}, respectively. We find that the interactions oscillate between FM and AFM behavior and decay exponentially with the impurity separation. For ε_{F_1}, in panels (a)–(d), J_{DM} decays much faster than the other components. The J_{xx} term is mostly FM, while the J_{zz} term is AFM for large separations. For ε_{F_2}, in panels (e)–(h), J_{xx} show the same qualitative behavior as J_{DM}, while the J_{zz} term has a longer period of oscillation than J_{xx} and J_{DM} interaction terms, and $J_{zz} > 0$ for $r/a > 30$ so that the impurities aligned antiferromagnetically for larger separation.

Figure 6 shows the distance dependence of indirect coupling between the impurities when the nanoribbon width is increased from $N = 7$ to $N = 13$. Two impurities localized with distance $\delta = -1$ from the nanoribbon center. The first impurity is fixed at the initial position and the second one moves along the horizontal line parallel to the center of nanoribbon towards edge. Two impurities hybridized to d_{z^2} orbitals. The two doping levels (52 and 106 holes) which shown in Fig. 6 are indicated in the bottom of the panels.

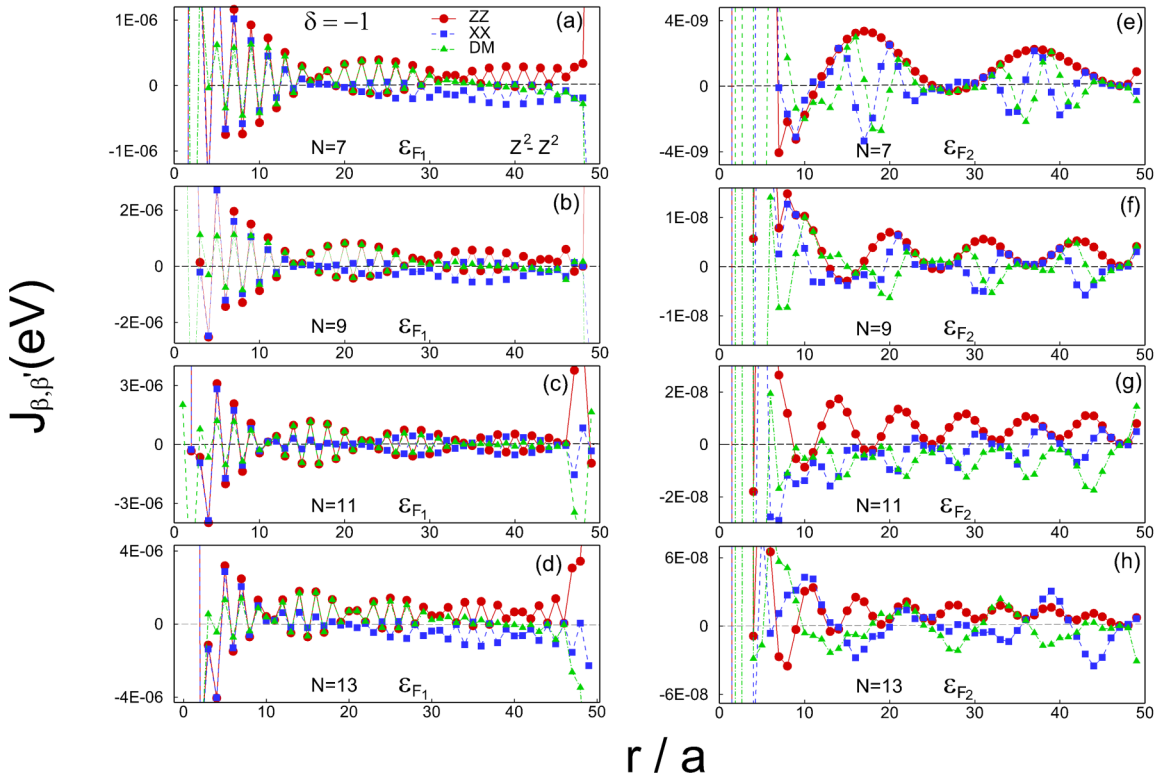

FIG. 6. The three components of the effective impurity interaction vs relative distance along the horizontal direction of the nanoribbon for different widths N and orbital d_{Z^2}. The impurities embedded at the on-site position with distance $\delta = -1$ from the center of the nanoribbon. The first impurity is fixed at the beginning of the selected row, while the second one moves at all onsites along the corresponding direction. The curves correspond to ε_{F1}, panels (a)–(d), and ε_{F2}, panels (e)–(h).

The three components (ZZ, XX, and DM) oscillate between AFM and FM behavior and have different oscillation patterns for two doping levels. These components in each panel of Fig. 6 have nearly the same period of oscillation, except for J_{ZZ} for a width of $N = 7$ and doping level ε_{F_2}, panel (e), that has a longer period of oscillation than J_{XX} and J_{DM}. We see that J^{z^2,z^2} for width $N = 7$, panels (a) and (e), shows the same behavior as $J^{x^2-y^2,x^2-y^2}$ and $J^{x^2-y^2,xy}$ that is described above. When the doping level is set to ε_{F_1}, the interaction has the same order of magnitude for all the nanoribbon widths. However, for ε_{F_2} the interaction first increases one order of magnitude, then it stays almost constant with width. We can see that the number of oscillation periods increases for both levels of doping by increasing the nanoribbon width, but with shorter periods of oscillation. For instance, J_{ZZ} for width $N = 7$ for ε_{F_1}, panel (a), has oscillation period nearly 16 sites, while for width $N = 13$ the period is about 10 sites. The number of oscillation periods for doping level ε_{F_2} is further than ε_{F_1} when the nanoribbon width increases. For all the studied nanoribbon widths, the strength of the indirect exchange interaction becomes weak for larger distances between impurities.

We analyze the effective exchange interaction as a function of the impurity separation for plaquette configuration for two doping levels corresponding to 52 and 106 holes in Figs. 7(a) and 7(b), respectively. The impurities localized in hollow sites below the symmetry axis are hybridized to d_{z^2} orbitals. The first impurity is held fixed at the initial plaquette position while the second impurity moves along the horizontal line parallel to the center of the nanoribbon as shown by dashed blue in Fig. 1. In the plaquette situation, each impurity is surrounded by three Mo atoms (in a triangle) which is considered in nearest-neighbor position. The exchange coupling associated to each of the Mo atoms is $J_0/3$. We find that J^{z^2,z^2} for plaquette configuration has similar oscillation behavior to the one described for onsite configuration, J^{z^2,z^2}, $J^{x^2-y^2,x^2-y^2}$, and $J^{x^2-y^2,xy}$. In panel (a), for ε_{F_1}, the different exchange components oscillate between AFM and FM behavior, and for larger separations, $r/a > 34$, $J_{ZZ} > 0$ and $J_{XX} < 0$, $J_{DM} < 0$. However, for doping level ε_{F_2}, panel (b), the Ising component $J_{ZZ} > 0$ for $r/a > 11$ and the other components oscillate always between AFM and FM. If we compare the plaquette configuration with onsite, Fig. 6 for $N = 7$, we observe that interaction for the plaquette case has a smaller magnitude than onsite. The interaction for ε_{F_1} is one order of magnitude smaller and for ε_{F_2} is slightly smaller in magnitude due to the contributions of the conduction electrons from the three first neighbor atoms, Mo atoms, around each impurity in the indirect exchange interaction.

In Fig. 8, we analyze the nanoribbon width dependence on the RKKY coupling for the fixed distance between the impurities which are localized in the center of the nanoribbon. Two impurities are hybridized to the $d_{x^2-y^2}$ orbital. The two doping levels, corresponding to 52 and 106 holes, are indicated at the bottom of the panels (a) and (b), respectively. It is visible that the coupling energy depends on the nanoribbon width, with a short period of oscillations, about two sites. The oscillations

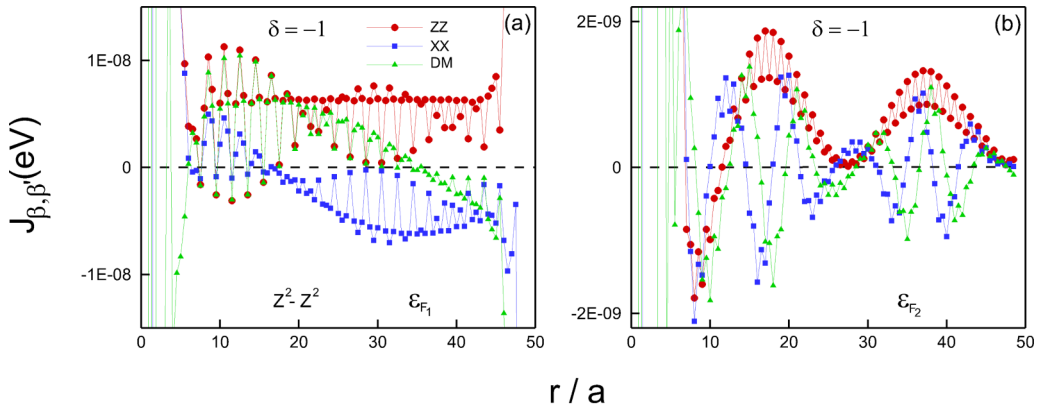

FIG. 7. The three components of the effective impurity interaction vs relative distance along the horizontal direction of the nanoribbon. The impurities embedded at plaquette position with distance $\delta = -1$ from the center of the nanoribbon. The first impurity is held fixed at the initial plaquette position and the second one moves at all plaquettes along the corresponding direction. The curves correspond to (a) ε_{F1} and (b) ε_{F2}. First and second impurities are assumed hybridized both to d_{z^2} orbitals.

decrease by the increasing nanoribbon width. If we compare the behavior of the interaction for two doping levels, panels (a) and (b), we observe that the oscillations decay slower with the width for ε_{F_2}. As one can observe in panel (a), first $J_{\rm DM}$ oscillates between FM and AFM behavior, then it stays always FM for $N \geqslant 9$. However, $J_{\rm ZZ}$ and $J_{\rm XX}$ interaction terms are AF for $N \leqslant 13$, alternating between AFM and FM as the width increases. In panel (b), the three components of the indirect exchange are always AF. The interaction for the $J_{\rm DM}$ term has smaller magnitude than the other components for two doping levels. In order to verify the correctness of the numerical results, we use perturbation theory calculation as a benchmark, at least for one example in Fig. 9 which shows RKKY interaction vs separation between two magnetic impurities localized in the bottom edge of the nanoribbon. We perform our calculations by second-order perturbation theory and compare with the exact diagonalization-based calculations. Panels (a) and (b) show two different doping levels which are represented by Fermi energies ε_{F_1} and ε_{F_2}, respectively. The two doping levels, corresponding to 52 and 106 holes, are indicated at the bottom of the panels. The Ising component of the indirect exchange term and the different exchange terms are indicated in panels (a) and (b), respectively. The first impurity is localized at the $r/a = 0$, while the second one is at the $r/a > 0$, up to $r/a = 49$. The exchange coupling between the localized magnetic moments is set to $J_0 = 10$ meV, and consider both impurities to be hybridized to d_{z^2} orbitals.

We can observe that the results obtained by the exact diagonalization-based calculation approach and by second-order perturbation theory are agreement for small J_{α_i} in equation (5). Two panels exhibit the oscillatory behavior of RKKY interaction, J^{z^2,z^2}, as described before for $J^{x^2-y^2,x^2-y^2}$ and $J^{x^2-y^2,xy}$, with natural quantitative differences on the overall amplitude, depending on the orbital to which impurities hybridize and the value of J_0. In Fig. 9, $J_{\rm ZZ}$ is mostly AFM (positive) in nature, but $J_{\rm XX}$ and $J_{\rm DM}$ oscillate always between AFM and FM. We find that the RKKY interaction envelope decays exponentially with distance r for two doping levels, although it decays slower at the deeper Fermi level in the gap (higher doping), ε_{F_2}, as described before for $J^{x^2-y^2,x^2-y^2}$ and $J^{x^2-y^2,xy}$.

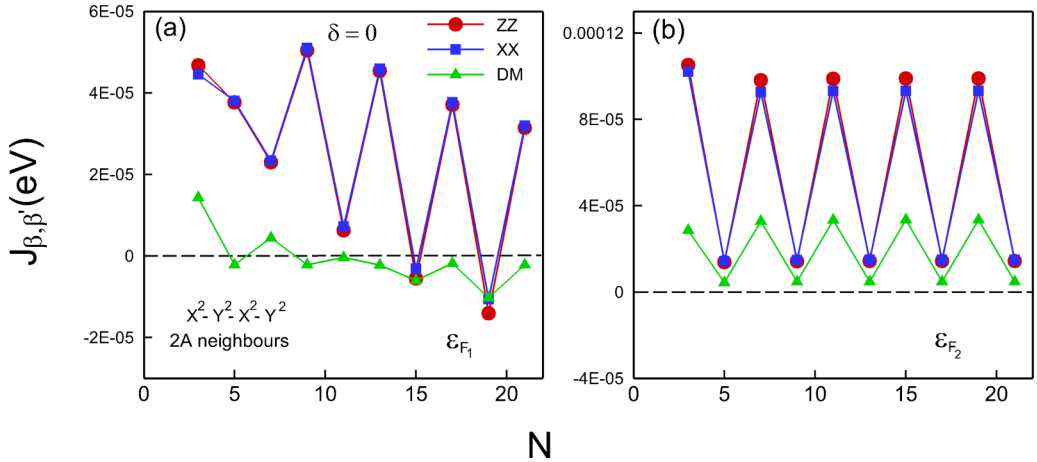

FIG. 8. The three components of the effective impurity interaction vs width of the nanoribbon. The curves correspond to (a) ε_{F1} and (b) ε_{F2}. The plots are presented for impurities located at the center of the nanoribbon. First and second impurities are assumed hybridized both to $d_{x^2-y^2}$ orbitals which are indicated in panel (a).

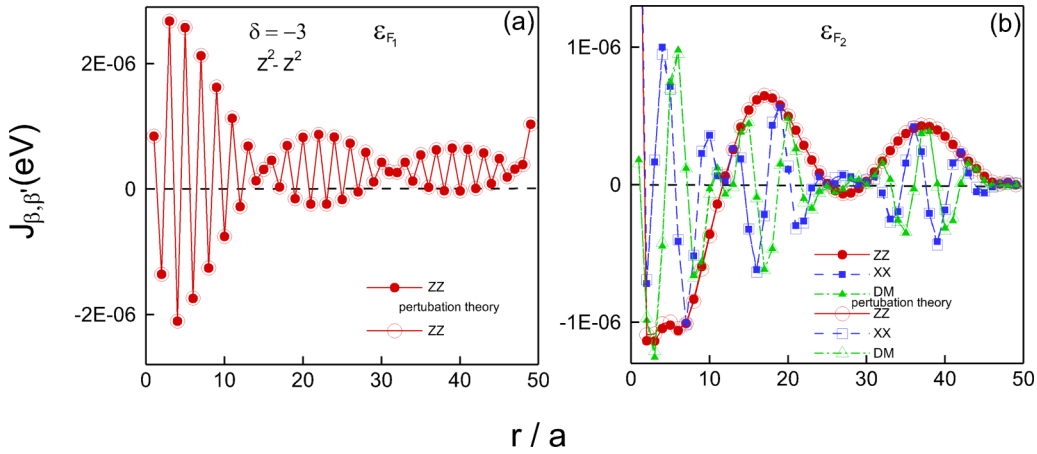

FIG. 9. The three components of the effective impurity interaction vs relative distance along the horizontal direction of the nanoribbon. The curves correspond to (a) ε_{F1} and (b) ε_{F2}. The plots are presented for impurities located at the edge of the nanoribbon. The interaction is calculated for $J(= 10$ meV). Full (empty) symbols indicate the exact diagonalization-based calculation approach (perturbation theory) results: red for Ising ZZ, blue for XX, and green for DM terms. First and second impurities are assumed hybridized both to d_{z^2} orbitals which are indicated in panel (a).

Let us discuss the behavior of the RKKY interaction for two doping levels as it contains different orbital and spatial symmetries. We observe that the three components of RKKY interaction (Ising, XX, and DM) oscillate between AFM and FM behavior and have different oscillation patterns for two doping levels. The overall decaying envelope and oscillation frequency depend smoothly on the Fermi energy value. The details of the oscillation periods naturally depend on the orbital to which impurities hybridize and distance of the impurity pair from the nanoribbon center. The RKKY interaction decays exponentially with the impurity separation along the symmetry axis of the nanoribbon, although it decays slower at the deeper Fermi level in the gap (higher doping). Moreover, when the impurities are located on the lower edge of the nanoribbon (such as away from the center of the nanoribbon), $\delta = -3$, the strength of the indirect interaction is relatively large, since the modulus squared of the wave function has large amplitude. For instance, in panel (d) of Fig. 3, for $\delta = -3$, we see that the indirect coupling has a larger magnitude than the other panels. Also, we can see this result in Figs. 4 and 5.

IV. CONCLUSIONS

We have studied the effective indirect interaction between two magnetic impurities localized in a p-doped MoS_2 nanoribbon in the presence of the intrinsic spin-orbit interaction. Our calculations are based on a three-orbital tight-binding model for a finite nanoribbon system with periodic boundary conditions. We analyzed the interaction for magnetic impurities situated at various distances ($\delta = -1, -2, -3$) from the system symmetry axis and on edges. The large spin-orbit coupling leads to the spatial anisotropy in the RKKY interaction amplitude and appearance of collinear and noncollinear terms. The DM interaction has the same order as the J_{XX} and Ising J_{ZZ} components. The magnitude of the indirect RKKY coupling between magnetic impurity spins in MoS_2 nanoribbon is strongly dependent on the location of the impurities in the nanoribbon. Also, the interaction $J^{\beta,\beta'}_{\alpha,\alpha'}$ between magnetic impurities hybridized to different orbitals exhibits pronounced oscillatory behavior which is naturally dependent on the energy doping. Thus, the magnitude of the interactions and the magnetic order of the system can be tuned by doping or gating of the material to a suitable midgap state and by the judicious position of magnetic impurities. Most interactions are nearly out of phase with each other, with similar periods of oscillation for ε_{F_1}. However, J_{ZZ} has a longer period of oscillation than other components for ε_{F_2}, with the intervalley scattering mechanisms responsible for this behavior. The magnitude of the RKKY interaction for magnetic impurities localized at nanoribbon edges is stronger than the center impurities. We find that the RKKY interaction is sensitive to the Fermi energy values and changes dramatically in p-doped MoS2 nanoribbon. The RKKY interaction envelope decays exponentially by increasing distance, however, more slowly for deeper Fermi levels (higher doping). In general, all coupling terms in the nanoribbon MoS_2 system depend on the separation direction between magnetic impurities, either horizontal or vertical, which shows the importance of crystal symmetries in the effective exchange interaction. In order to verify the correctness of the numerical results in the paper, we use perturbation theory calculation as a benchmark, at least for one example. We observed that the results obtained by the exact diagonalization-based calculation approach and by second-order perturbation theory are in agreement for small J_{α_i} in equation (5) [69–73].

[1] K. Novoselov, D. Jiang, F. Schedin, T. Booth, V. Khotkevich, S. Morozov, and A. Geim, Proc. Natl. Acad. Sci. **102**, 10451 (2005).

[2] G.-B. Liu, D. Xiao, Y. Yao, X. Xu, and W. Yao, Chem. Soc. Rev. **44**, 2643 (2015).

[3] Q. H. Wang, K. Kalantar-Zadeh, A. Kis, J. N. Coleman, and M. S. Strano, Nat. Nanotechnol. **7**, 699 (2012).

[4] X. Xu, W. Yao, D. Xiao, and T. F. Heinz, Nat. Phys. **10**, 343 (2014).

[5] H. Li, J. Wu, Z. Yin, and H. Zhang, Acc. Chem. Res. **47**, 1067 (2014).

[6] G. Eda, H. Yamaguchi, D. Voiry, T. Fujita, M. Chen, and M. Chhowalla, Nano Lett. **11**, 5111 (2011).

[7] C. Gong, C. Huang, J. Miller, L. Cheng, Y. Hao, D. Cobden, J. Kim, R. S. Ruoff, R. M. Wallace, K. Cho *et al.*, ACS Nano **7**, 11350 (2013).

[8] W. Zhang, J.-K. Huang, C.-H. Chen, Y.-H. Chang, Y.-J. Cheng, and L.-J. Li, Adv. Mater. **25**, 3456 (2013).

[9] H. Schmidt, S. Wang, L. Chu, M. Toh, R. Kumar, W. Zhao, A. Castro Neto, J. Martin, S. Adam, B. Özyilmaz *et al.*, Nano Lett. **14**, 1909 (2014).

[10] Y.-H. Lee, X.-Q. Zhang, W. Zhang, M.-T. Chang, C.-T. Lin, K.-D. Chang, Y.-C. Yu, J. T.-W. Wang, C.-S. Chang, L.-J. Li *et al.*, Adv. Mater. **24**, 2320 (2012).

[11] M. Chhowalla, H. S. Shin, G. Eda, L.-J. Li, K. P. Loh, and H. Zhang, Nat. Chem. **5**, 263 (2013).

[12] X. Zhang, X.-F. Qiao, W. Shi, J.-B. Wu, D.-S. Jiang, and P.-H. Tan, Chem. Soc. Rev. **44**, 2757 (2015).

[13] R. Ganatra and Q. Zhang, ACS nano **8**, 4074 (2014).

[14] Y. Wang, S. Li, and J. Yi, Sci. Rep. **6**, 24153 (2016).

[15] B. W. Baugher, H. O. Churchill, Y. Yang, and P. Jarillo-Herrero, Nano Lett. **13**, 4212 (2013).

[16] A. Castellanos-Gomez, M. Poot, G. A. Steele, H. S. van der Zant, N. Agraït, and G. Rubio-Bollinger, Adv. Mater. **24**, 772 (2012).

[17] N. Singh, G. Jabbour, and U. Schwingenschlögl, Eur. Phys. J. B **85**, 392 (2012).

[18] Y. Yoon, K. Ganapathi, and S. Salahuddin, Nano Lett. **11**, 3768 (2011).

[19] Q. Yue, J. Kang, Z. Shao, X. Zhang, S. Chang, G. Wang, S. Qin, and J. Li, Phys. Lett. A **376**, 1166 (2012).

[20] K. F. Mak, C. Lee, J. Hone, J. Shan, and T. F. Heinz, Phys. Rev. Lett. **105**, 136805 (2010).

[21] S. Tongay, S. S. Varnoosfaderani, B. R. Appleton, J. Wu, and A. F. Hebard, Appl. Phys. Lett. **101**, 123105 (2012).

[22] L. Cai, J. He, Q. Liu, T. Yao, L. Chen, W. Yan, F. Hu, Y. Jiang, Y. Zhao, T. Hu *et al.*, J. Am. Chem. Soc. **137**, 2622 (2015).

[23] J. Klinovaja and D. Loss, Phys. Rev. B **88**, 075404 (2013).

[24] Y. Li, H. Wang, L. Xie, Y. Liang, G. Hong, and H. Dai, J. Am. Chem. Soc. **133**, 7296 (2011).

[25] H. I. Karunadasa, E. Montalvo, Y. Sun, M. Majda, J. R. Long, and C. J. Chang, Science **335**, 698 (2012).

[26] X. Gu, W. Cui, H. Li, Z. Wu, Z. Zeng, S.-T. Lee, H. Zhang, and B. Sun, Adv. Energy Mater. **3**, 1262 (2013).

[27] T. Stephenson, Z. Li, B. Olsen, and D. Mitlin, Energ. Environ. Sci. **7**, 209 (2014).

[28] Y. Li, Z. Zhou, S. Zhang, and Z. Chen, J. Am. Chem. Soc. **130**, 16739 (2008).

[29] A. R. Botello-Méndez, F. Lopez-Urias, M. Terrones, and H. Terrones, Nanotechnology **20**, 325703 (2009).

[30] S. Power and M. Ferreira, Crystals **3**, 49 (2013).

[31] K. Szałowski, J. Phys.: Condens. Matter **25**, 166001 (2013).

[32] A. M. Black-Schaffer, Phys. Rev. B **81**, 205416 (2010).

[33] A. Akbari-Sharbaf, J. Appl. Phys. **116**, 194309 (2014).

[34] A. Mirehi and E. Heidari-Semiromi, Phys. Lett. A **382**, 2831 (2018).

[35] A. Mirehi and E. Heidari-Semiromi, Phys. Chem. Chem. Phys. (2019).

[36] F. Parhizgar, H. Rostami, and R. Asgari, Phys. Rev. B **87**, 125401 (2013).

[37] H. Hatami, T. Kernreiter, and U. Zulicke, Phys. Rev. B **90**, 045412 (2014).

[38] D. Mastrogiuseppe, N. Sandler, and S. E. Ulloa, Phys. Rev. B **90**, 161403(R) (2014).

[39] O. Ávalos-Ovando, D. Mastrogiuseppe, and S. E. Ulloa, Phys. Rev. B **93**, 161404(R) (2016).

[40] O. Ávalos-Ovando, D. Mastrogiuseppe, and S. E. Ulloa, J. Phys.: Condens. Matter **30**, 045801 (2018).

[41] R. Mishra, W. Zhou, S. J. Pennycook, S. T. Pantelides, and J.-C. Idrobo, Phys. Rev. B **88**, 144409 (2013).

[42] A. N. Andriotis and M. Menon, Phys. Rev. B **90**, 125304 (2014).

[43] S.-C. Lu and J.-P. Leburton, Nanoscale Res. Lett. **9**, 676 (2014).

[44] W. Cong, Z. Tang, X. Zhao, and J. Chu, Sci. Rep. **5**, 9361 (2015).

[45] H. Shu, P. Luo, P. Liang, D. Cao, and X. Chen, ACS Appl. Mater. Interfaces **7**, 7534 (2015).

[46] J. Vähäkangas, P. Lantto, J. Vaara, M. Huttula, and W. Cao, Chem. Commun. **53**, 5428 (2017).

[47] K. Dolui, I. Rungger, C. D. Pemmaraju, and S. Sanvito, Phys. Rev. B **88**, 075420 (2013).

[48] O. Ávalos-Ovando, D. Mastrogiuseppe, and S. E. Ulloa, Phys. Rev. B **94**, 245429 (2016).

[49] S. Pavlović and F. M. Peeters, Phys. Rev. B **91**, 155410 (2015).

[50] G.-B. Liu, W.-Y. Shan, Y. Yao, W. Yao, and D. Xiao, Phys. Rev. B **88**, 085433 (2013).

[51] R. Bromley, R. Murray, and A. Yoffe, J. Phys. C **5**, 759 (1972).

[52] L. Mattheiss, Phys. Rev. B **8**, 3719 (1973).

[53] Z. Zhu, Y. Cheng, and U. Schwingenschlögl, Phys. Rev. B **84**, 153402 (2011).

[54] E. S. Kadantsev and P. Hawrylak, Solid State Commun. **152**, 909 (2012).

[55] S. Lebegue and O. Eriksson, Phys. Rev. B **79**, 115409 (2009).

[56] C. Ataca, H. Sahin, and S. Ciraci, J. Phys. Chem. C **116**, 8983 (2012).

[57] D. Xiao, G.-B. Liu, W. Feng, X. Xu, and W. Yao, Phys. Rev. Lett. **108**, 196802 (2012).

[58] L. Sun, J. Yan, D. Zhan, L. Liu, H. Hu, H. Li, B. K. Tay, J.-L. Kuo, C.-C. Huang, D. W. Hewak *et al.*, Phys. Rev. Lett. **111**, 126801 (2013).

[59] N. Alidoust, G. Bian, S.-Y. Xu, R. Sankar, M. Neupane, C. Liu, I. Belopolski, D.-X. Qu, J. D. Denlinger, F.-C. Chou *et al.*, Nat. Commun. **5**, 4673 (2014).

[60] J. A. Miwa, S. Ulstrup, S. G. Sørensen, M. Dendzik, A. G. Čabo, M. Bianchi, J. V. Lauritsen, and P. Hofmann, Phys. Rev. Lett. **114**, 046802 (2015).

[61] J. Qi, X. Li, Q. Niu, J. Feng *et al.*, Phys. Rev. B **92**, 121403(R) (2015).

[62] M. Saab and P. Raybaud, J. Phys. Chem. C **120**, 10691 (2016).

[63] M. A. Ruderman and C. Kittel, Phys. Rev. **96**, 99 (1954).

[64] T. Kasuya, Prog. Theor. Phys. **16**, 45 (1956).

[65] K. Yosida, Phys. Rev. **106**, 893 (1957).

[66] H. Imamura, P. Bruno, and Y. Utsumi, Phys. Rev. B **69**, 121303(R) (2004).
[67] V. I. Litvinov and V. K. Dugaev, Phys. Rev. B **58**, 3584 (1998).
[68] B. Fischer and M. W. Klein, Phys. Rev. B **11**, 2025 (1975).
[69] J. Duffy, P. Gorman, S. Power, and M. Ferreira, J. Phys.: Condens. Matter **26**, 055007 (2013).
[70] C. Kittel, *Solid state physics*, Vol. 22, edited by F. Seitz, D. Turnbull, and H. Ehrenreich (1968).
[71] Y. Yafet, Phys. Rev. B **36**, 3948 (1987).
[72] G. F. Giuliani, G. Vignale, and T. Datta, Phys. Rev. B **72**, 033411 (2005).
[73] J. Alfonsi and M. Meneghetti, New J. Phys. **14**, 053047 (2012).